PHOTONICS Research

Promoting spintronic terahertz radiation via Tamm plasmon coupling

Yunqing Jiang,[1,2,†] Hongqing Li,[2,3,†] Xiaoqiang Zhang,[1,2,*] Fan Zhang,[1,2] Yong Xu,[1,2] Yongguang Xiao,[3] Fengguang Liu,[1,2] Anting Wang,[4] Qiwen Zhan,[5] and Weisheng Zhao[1,2]

[1]School of Integrated Circuit Science and Engineering, Hefei Innovation Research Insititute, Beihang University, Beijing 100191, China
[2]Anhui High Reliability Chips Engineering Laboratory, Hefei 230013, China
[3]School of Materials Science and Engineering, Xiangtan University, Xiangtan 411105, China
[4]Department of Optics and Optical Engineering, University of Science and Technology of China, Hefei 230026, China
[5]School of Optical-Electrical and Computer Engineering, University of Shanghai for Science and Technology, Shanghai 200093, China
[†]These authors contributed equally to this work.
*Corresponding author: xqzhang@buaa.edu.cn

Received 17 February 2023; revised 23 April 2023; accepted 26 April 2023; posted 26 April 2023 (Doc. ID 487711); published 26 May 2023

Spectral fingerprint and terahertz (THz) field-induced carrier dynamics demands the exploration of broadband and intense THz signal sources. Spintronic THz emitters (STEs), with high stability, a low cost, and an ultrabroad bandwidth, have been a hot topic in the field of THz sources. One of the main barriers to their practical application is lack of an STE with strong radiation intensity. Here, through the combination of optical physics and ultrafast photonics, the Tamm plasmon coupling (TPC) facilitating THz radiation is realized between spin THz thin films and photonic crystal structures. Simulation results show that the spectral absorptance can be increased from 36.8% to 94.3% for spin THz thin films with TPC. This coupling with narrowband resonance not only improves the optical-to-spin conversion efficiency, but also guarantees THz transmission with a negligible loss (~4%) for the photonic crystal structure. According to the simulation, we prepared this structure successfully and experimentally realized a 264% THz radiation enhancement. Furthermore, the spin THz thin films with TPC exhibited invariant absorptivity under different polarization modes of the pump beam and weakening confinement on an obliquely incident pump laser. This approach is easy to implement and offers possibilities to overcome compatibility issues between the optical structure design and low energy consumption for ultrafast THz optospintronics and other similar devices.

https://doi.org/10.1364/PRJ.487711

1. INTRODUCTION

Spintronic terahertz emitters (STEs), with high stability, a low cost, an ultrabroad bandwidth, and controllable polarization, have come a long way since the early days of this topic and show promising applications in communications, medicine, and imaging [1–6]. In terms of integration and miniaturization, one of the limitations is the emission intensity in a practical application. Especially for terahertz (THz) sources in information technology and quantum devices [7–11], there is a necessary requirement for highly efficient STEs: the low dissipation of energy. Some improvements for spintronic THz radiation enhancement have been surveyed; for example, searching for the interface state, the spin Hall angle, the index of refraction, and the absorption of layers. Luo *et al.* reported that the THz radiation can be generated from Bi_2Se_3 and Cu-doped Bi_2Se_3 single crystals. Due to the contribution of the Dirac fermions of the surface state, the THz amplitude is enhanced 50 times [12]. Compared to heavy metals, topological insulators have a large spin Hall angle and higher spin to charge conversion efficiency [13]. Using a topological insulator to replace traditional metals has become one of possible approaches to enhance THz radiation [14,15]. However, building a topological material is extremely difficult not only because of the complicated technology but also because of the theoretical limitations. On the other hand, the optical utilization rate is not very high due to the thinness of the film, especially for topological materials, meaning that most of the pump energy is wasted. Therefore, trade-offs are necessary between the thickness of the film and the light absorptivity. Using surface plasmonic polaritons (SPPs) is a good way to enhance the localized pump laser intensity [16–19]. Although nanoplasmonic technology for THz radiation enhancement has a few limitations, the idea is a good way forward that combines optical physics and ultrafast spintronics.

Optical structures can be easily accomplished with a vast choice of materials and manufacturing technology, as well as greater expandability [20–22]. Recently, excellent optical gain

properties have been explored, such as bound state in the continuum (BIC) resonances [23], epsilon-near-zero (ENZ) films [24], and 1D photonic crystals [21,25–27]. Hybridizing a metasurface with ENZ films has emerged as a promising alternative to promote THz radiation and shape the THz polarization [24]. Due to the weak compatibility and complicated manufacture process, however, it is difficult to widely use in other kinds of THz emitters. In terms of BIC resonances, it can cause strong electromagnetic resonances in low ohmic loss materials like lithium niobate but is difficult to use on metal materials with high ohmic loss. Similarly, ENZ films are very limited on materials that have weak THz radiation. Alternating periodic multilayers via different refractive indexes can create a photonic band gap along the propagation direction when it satisfies the special optical confining condition [28]. Note that the photonic band gap has an excellent filter property; i.e., an increased sensitivity against an unwanted wavelength. Based on Maxwell's equations, the band of a photonic crystal can be calculated and adjusted. As a result, photonic crystals have emerged as excellent reflectors when designing an optical structure against a specific wavelength of incident light. Related approaches that rely on planar metal and dielectric heterostructures have resulted in a few potentially viable strategies for light absorptivity, such as Tamm plasmon coupling (TPC) [29–31]. In this state, most of the light radiation is trapped on the metal/dielectric interface and is absorbed by the metal. Unlike the SPP that has been found in spin-thin films and a dielectric layer with a complicated structure (e.g., prisms [32]), TPC can be excited directly between the metal/dielectric interface [33]. For TPC, most of the existing methods for strong absorptivity of the incident light require a thick metal [34]. However, in terms of spintronics THz emission, it has an optimal thickness of the STE within several nanometers, resulting in a low absorptivity of the pump laser [35,36]. A method that offers strong absorptivity and optimal thickness of the STE, however, remains elusive, despite several potential applications.

In this paper, we created a photonic nanostructure design for TPC between the spin THz thin films and a 1D photonic crystal using a simple manufacturing technology. The spin thin films can act as both the THz emitter and planar metal for the TPC structure. The simulation and experimental results show that a 94.3% narrow absorptance spectrum at 780 nm and a broad transmissivity (~96%) in the THz range are obtained. Compared to pure spin thin films, spin thin films with TPC directly excited THz radiation with a 264% improvement without polarization mode confinement. Our approach enables modulation of the center of the incident laser wavelength for diverse scenarios by adjusting the dielectric properties, such as the refractive index of the dielectric and the insert layer's thickness.

2. RESULTS AND DISCUSSION

As shown in Fig. 1(a), the STE with TPC is composed of a 1D photonic crystal (SiO_2 and Si_3N_4) and spin thin films (Pt/Co/MgO). When the pump beam is incident from the left of the spin thin films, the reflection coefficient for the incident light propagating to the spin thin films from the side of the 1D photonic crystal to the spin thin films is r_1, the reflection coefficient of a wave incident on the dielectric layers from just after the spin thin films is r_2, and these two reflection coefficients can be calculated by the transfer matrix method. More details can be found in Appendix A. In the simulations, the refractive indexes of Co, Pt, and MgO are adopted from Refs. [37–39]. The refractive indexes of SiO_2 and Si_3N_4 are 1.446 and 1.99, respectively. The dielectric layers are composed of 20 groups of alternately stacked Si_3N_4 and SiO_2 with thicknesses of 92 nm and 113 nm, respectively. Then the intrinsic mode field in the

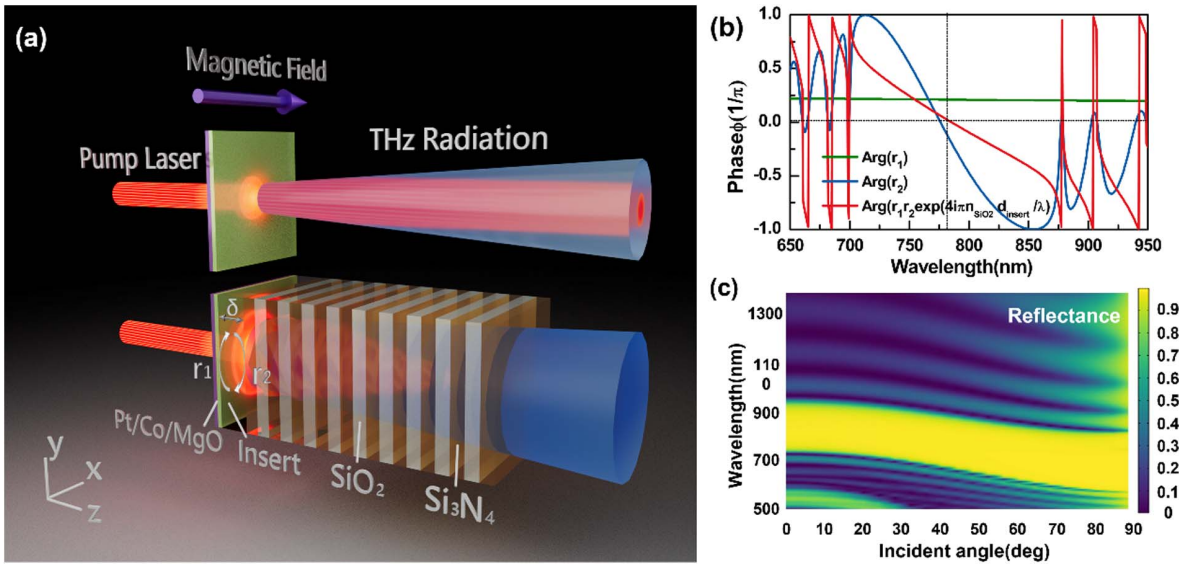

Fig. 1. (a) Schematic illustration of the spin thin films without TPC and with TPC structure for THz radiation. (b) Phase of r_1, r_2, and $r_1 r_2 \exp[i(4\pi n_{SiO_2} d_{insert})/\lambda]$ as a function of wavelength, when the thickness of the optical cavity is 57 nm. (c) Simulated reflectance spectra of the dielectric layers as a function of incidence angle and wavelength for TM polarization.

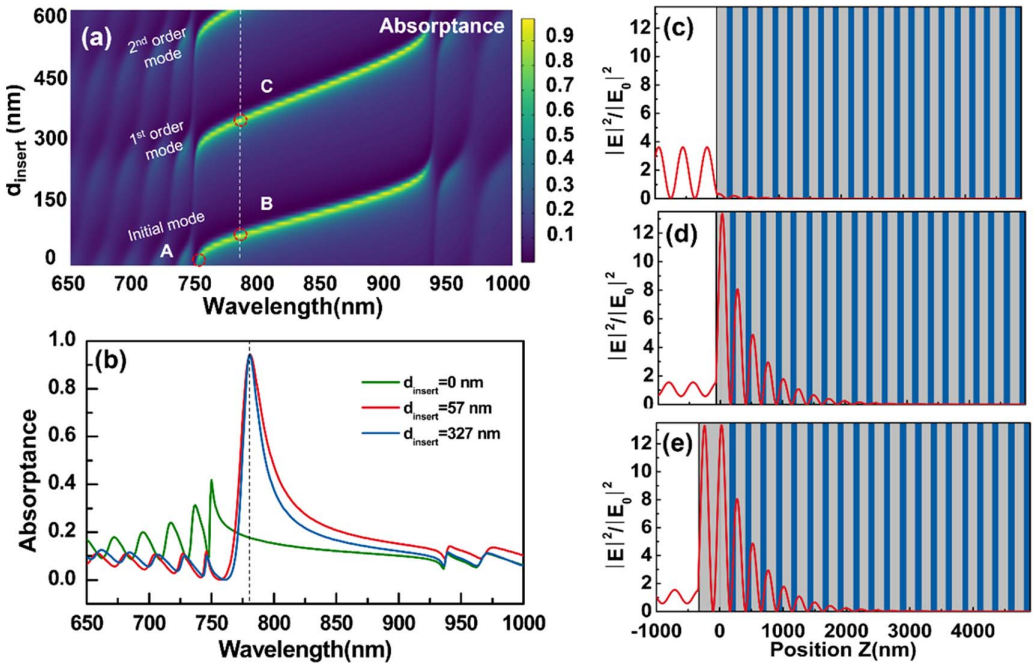

Fig. 2. (a) Simulated absorptance varying with SiO_2 cavity thickness d_{insert} and optical wavelength. (b) Absorptance spectra with different d_{insert} ($d_{\text{insert}} = 0$ nm, 57 nm, 327 nm). (c)–(e) Normalized electric field profile distributions of point A ($d_{\text{insert}} = 0$ nm, $\lambda = 743$ nm), point B ($d_{\text{insert}} = 57$ nm, $\lambda = 780$ nm), and point C ($d_{\text{insert}} = 327$ nm, $\lambda = 780$ nm), respectively.

insert cavity layer can be represented by the transfer matrix [40,41]

$$A\begin{pmatrix}1\\ r_1\end{pmatrix} = \begin{pmatrix}\exp(i\delta) & 0\\ 0 & \exp(-i\delta)\end{pmatrix}\begin{pmatrix}r_2\\ 1\end{pmatrix}, \tag{1}$$

where A is a constant and δ is the phase change between the interfaces, which is equal to $4\pi n_{SiO_2} d_{\text{insert}}/\lambda$. After some calculations and simplicities, the excitation condition can be obtained as

$$r_1 r_2 \exp(2i\delta) \approx 1. \tag{2}$$

Thus, the phase match condition for the excitation of the TPC is

$$\text{Arg}[r_1 r_2 e^{i(4\pi n_{SiO_2} d_{\text{insert}})/\lambda}] \approx 2\pi N, N = 0, 1, 2\ldots, \tag{3}$$

where λ is the incident wavelength; d_{insert} is the thickness of the SiO_2 insert layer, and its refractive index and thickness are n_{SiO_2} and 57 nm, respectively. The THz signal increases with an increase in the thickness of the nonferromagnetic metal layers and then reaches saturation, no longer increasing with a further increase in the thickness. However, with an increase in the ferromagnetic layer thickness, there is a trend of first increasing and then decreasing after a peak. With an increase in the total thickness of the spin thin films, the absorptance for the pump laser increases but the spin to charge conversion efficiency decreases sharply after a peak [36,42]. Therefore, the thicknesses of Pt and Co are both selected as 4 nm, respectively. Future research can still reference this method to further improve the THz signal by adjusting the parameters of the dielectric layers when stronger THz signal materials appear. For the sake of THz emission, the thickness of MgO film is 4 nm. Figure 1(b) shows the relationship between the phase of r_1, r_2, and $r_1 r_2 e^{[i(\frac{4\pi n_{SiO_2} d_{\text{insert}}}{\lambda})]}$ under different wavelengths. It can be seen that the phase is satisfied in Eq. (3) at the wavelength of 780 nm, and that $\text{Arg}\{r_1 r_2 e^{[i(\frac{4\pi n_{SiO_2} d_{\text{insert}}}{\lambda})]}\}$ is approximated to 0. As shown in Fig. 1(c), the dielectric layers have a band gap against an unwilling pump laser from 750 nm to 850 nm. Notably, the reflectance from any incident angles for the wavelength of a 780 nm laser can be up to 98%, resulting in the product of $|r_1|$ and $|r_2|$ being approximately 1. Thus, the perfect absorptance generated by the excitation of the TPC has been verified. In addition, the simulated transmittance for the THz wave on the dielectric layers obtains 95% and 96.35% within 2 THz (see Fig. 6 in Appendix B). This result indicates that the structure can be an excellent filter against a pump laser but not for a THz wave, as illustrated in Fig. 1(a).

From the analysis above, it is easy to find that the thickness of the insert layer can affect the resonance wavelength of the TPC. By varying the thickness of the insert layer from 0 nm to 600 nm, the optical absorptance from 750 nm to 950 nm can be adjusted, as shown in Fig. 2(a). With the continuous increase of d_{insert}, the optical absorptance caused by TPC has a periodic change that is related to the resonant mode of the insert layer, as expressed by [43]

$$d_{\text{insert}} = \frac{N\lambda}{2n_{SiO_2}}, \tag{4}$$

where N is the const in Eq. (3). In Fig. 2(a), three TPC modes can be found. When no insert exists ($d_{\text{insert}} = 0$), the initial

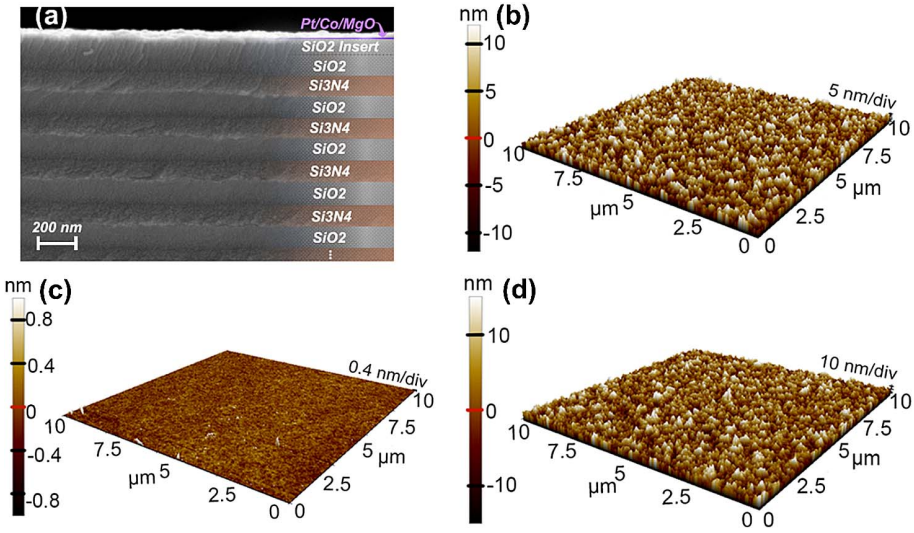

Fig. 3. (a) Cross-sectional SEM image of the spin thin films with a TPC structure. The average roughness of (b) spin thin films with TPC, (c) pure spin thin films, and (d) pure dielectric layers surface.

mode of the TPC is excited at the wavelength of 750 nm (point *A*). As the thickness of the insert is increased from zero to 57 nm, the phase shift induced by the insert generates a red shift of the resonance wavelength to 780 nm (point *B*). If the thickness of the insert is increased unceasingly, the higher order mode of the TPC can be excited sufficiently, as shown by the point *C* in Fig. 2(a). Thus, by tuning the thickness of the insert, the resonance wavelength of the TPC can be adjusted.

After adding the proper insert layer, a narrow and high resonance absorption can be generated at 780 nm corresponding to the wavelength of the pump beam. Figure 2(b) shows the absorptance spectra with different d_{insert}. As Fig. 2(b) shows, a weak resonance absorption at the wavelength of 750 nm can be found when the thickness of the insert is 0. Moreover, the absorptance can be as high as 94.38% at 780 nm, when the thickness of the insert is increased to $d_{\text{insert}} = 57$ nm. Figures 2(c)–2(e) illustrate the normalized profile electric field distributions of points *A*, *B*, and *C*. Note that the normalized electric field distributions are up to four times greater at point *B* than at point *A*, indicating the energy is well trapped at point *B*. This is because point *A* lies at the edge of the band gap of the 1D photonic crystal. Figures 2(d) and 2(e), show that point *C* is comparable to point *B* in its ability to generate TPC, and they correspond to the odd mode and even mode of the TPC, respectively. Considering the economical fabrication accessibility, a SiO_2 insert layer with a thickness of 57 nm is finally chosen. To investigate the optimal groups of alternating layers, we simulated the electric field distribution under different groups, as shown in Fig. 7 in Appendix C. With the increment of alternating layers, the electric field intensity increases before 20 groups, but approaches saturation after that number of groups. Thus, 20 groups of alternating layers are selected as a balanced consideration between the optical performance and simple preparation are discussed below.

After making a trade-off between spin to charge conversion efficiency and optical cavity performance, the well-defined alternating layers were prepared. To prepare the Tamm plasmon-enhanced STE, the 1D photonic crystal dielectric multilayer consisting of an insert layer (SiO_2) and 20 groups of alternating layers (SiO_2 and Si_3N_4) was first fabricated by plasma-enhanced chemical vapor deposition (PECVD). Then, the spin thin films (Pt/Co/MgO) for THz emission were deposited on the top of the dielectric layers using magnetron sputtering. At the same time, for comparison, pure spin thin films Pt/Co/MgO without TPC were prepared by magnetron sputtering. Figure 3(a) shows the cross-sectional SEM image of the spin thin films with a TPC structure. It is clear that a good homogeneity in the layer thicknesses and no layer interpenetration exist, which assures that the TPC structure will have an excellent optical gain property. The average thicknesses of SiO_2 and Si_3N_4 are, respectively, about 120 nm and 93 nm. For the sake of THz emission, a 4 nm MgO film was deposited between the Pt/Co and dielectric layers. It can buffer the roughness of dielectric layers from PECVD. Figures 3(b)–3(d) show the average roughness of different samples using an AFM. The average roughnesses of the spin thin films with a TPC structure, the pure spin thin films, and the pure dielectric layers surface are, respectively, 4.29 nm, 0.16 nm, and 4.85 nm. It is easy to see that the roughness of pure dielectric layers is obviously smoothened by the buffer layer.

Next, the performance of all samples was tested on a home-built THz time-domain spectroscopy system. A femtosecond pump laser (Spectra-Physics) with a repetition rate of 1 kHz, a central wavelength of 780 nm, and a pulse duration of 50 fs was used to pump the spintronic THz emission. A couple of permanent magnets used for in-plane magnetization along the *x* axis acted on the spintronic samples, as illustrated in Fig. 1(a), and provided 20 mT of the centric magnetic field. Using a 1 mm thick ZnTe electrooptic crystal, the spintronics THz radiation can be detected by a balanced detector. All the experiments were performed at room temperature and in a

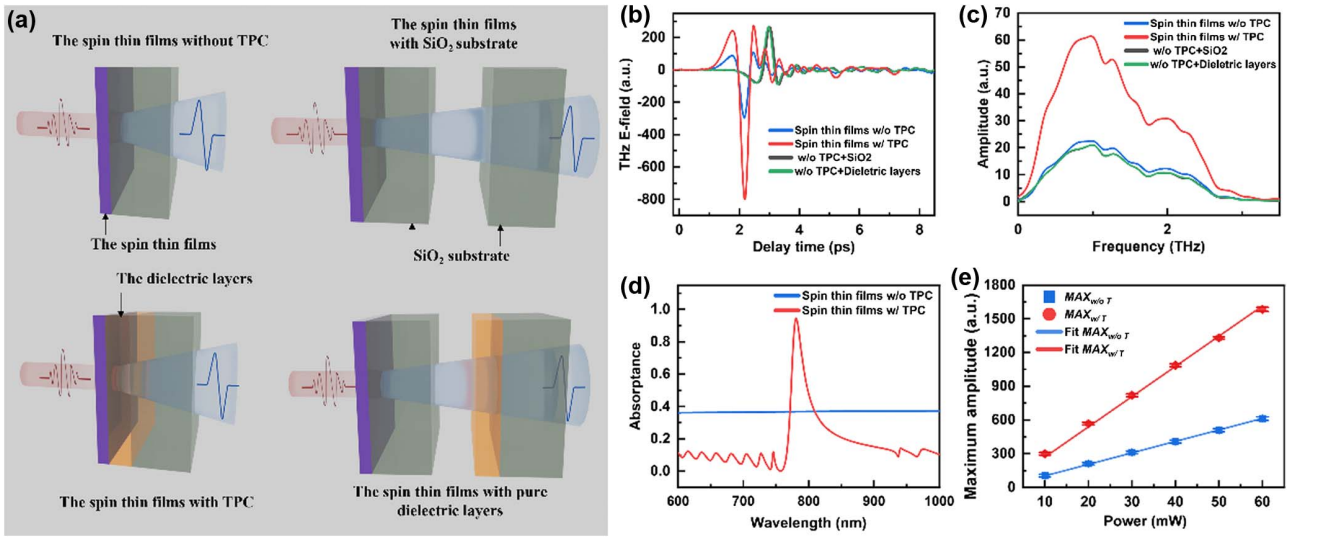

Fig. 4. (a) Illustration of four comparison experiments of pure spin thin films without TPC, spin thin films with TPC, spin thin films with SiO_2 substrate (without TPC + SiO_2), spin thin films with pure dielectric layers (without TPC + dielectric layers). (b) THz waveforms and (c) the frequency-domain THz signals from the spin thin films without TPC (blue line, MAX is 406), the spin thin films with TPC (red line, MAX is 1072), without TPC + SiO_2 (black line, MAX is 354), and without TPC + dielectric layers (green line, MAX is 356) at the pump fluence of 12.7 μJ/cm^2. (d) Simulation absorptance spectra of the spin thin films with TPC and without TPC. (e) Maximum amplitude of generated THz electric field as a function of the pump laser power when its spot diameter is 1 cm.

N_2 environment. In our THz experiments, four comparison experiments were considered. Their illustrations are exhibited in Fig. 4(a), where the pump laser is located on the side of spin thin films and the THz radiation is detected after all samples and substrates. To ensure the accuracy of the results, all THz TDS measurements were repeatedly tested. In Fig. 4(a), two of THz waveforms were generated by the pure spin thin films without TPC, and the spin thin films with TPC, respectively. The other two THz waveforms were generated by the pure spin thin films and then passed through one SiO_2 substrate (without TPC + SiO_2) or dielectric layers deposited on a SiO_2 substrate (without TPC + dielectric layers), respectively. There are two reasons why one SiO_2 substrate was used for comparison after the pure spin thin films: i) the dielectric layers are deposited at the SiO_2 substrate and ii) the SiO_2 substrate has an absorptance of 12.7% for the THz signal, as shown in Fig. 4(b). Excluding these irrelevant variables, the SiO_2 substrate was used to verify that the pure dielectric layers had no negative effects on the THz radiation. In Fig. 4(b), we found that the dielectric layers have little influence on the transmission of the generated THz wave, and it conformed to the simulation, as shown in Fig. 6 in Appendix B. As illustrated in Fig. 4(b), the pure dielectric layers also cannot enhance the THz radiation. Hence, it confirms that spin thin films with TPC structures play a crucial role in THz radiation enhancement.

Figures 4(b) and 4(c) display the THz time-domain waveforms and the respective magnitude in frequency domain from the four samples. As shown in Fig. 4(c), our samples can obtain a 3 THz bandwidth. By contrast, the THz waveforms and bandwidth remain unchanged between the spin thin films with TPC or not, except for a stronger THz amplitude from the spin thin films with TPC. It means the dielectric layers have little influence on the frequency of the THz waves, which is supported by the simulation results in Fig. 6 in Appendix B. To survey the properties of the samples quantificationally, the value of the peak-to-peak THz electric field is defined as the maximum amplitude (MAX). Here, the maximum amplitudes of the spin thin films with TPC and without TPC are $MAX_{w/T}$ and $MAX_{w/oT}$, respectively. $MAX_{w/oT}$ is 406 at the pump fluence of 12.7 μJ/cm^2, as shown in Fig. 4(b), while $MAX_{w/T}$ can achieve 1072 with TPC enhancement at the same pump fluence. Strikingly, we observed a predictable 264% enhancement in the spin thin films samples by comparing their maximum amplitude and frequency domain spectra. The normalized THz amplitudes of 0.5 mm ZnTe, spin thin films without TPC and with TPC are compared in Fig. 8 in Appendix D. Note that spin thin films with TPC have an approximate value compared to the 0.5 mm thick ZnTe THz emitter. The enhancement of the THz electric field is caused by the absorption dependence of incident pump laser according to [36]

$$E_{\mathrm{THz}} = Ze \int \mathrm{d}z \gamma j_s(d_{\mathrm{FM}}), \tag{5}$$

where $\frac{1}{Z}$ is the effective conductance of a parallel connection of all metal layers shunted by the adjacent substrate and air half-spaces, e is the elementary charge, γ is spin Hall angle, and $j_s(d_{\mathrm{FM}})$ is the spin current density directly after the ferromagnetic layer. Here, $j_s(d_{\mathrm{FM}}) \propto P_{\mathrm{abs}}$ where P_{abs} is the absorptance of the incident pump power [36]. Theoretical optical simulation confirms that our approach with TPC results in an absorptance enhancement for pump laser on the spin thin films. As shown in Fig. 4(d), an obvious absorption peak reaches 0.943 at 780 nm on the simulation absorptance spectra of the spin

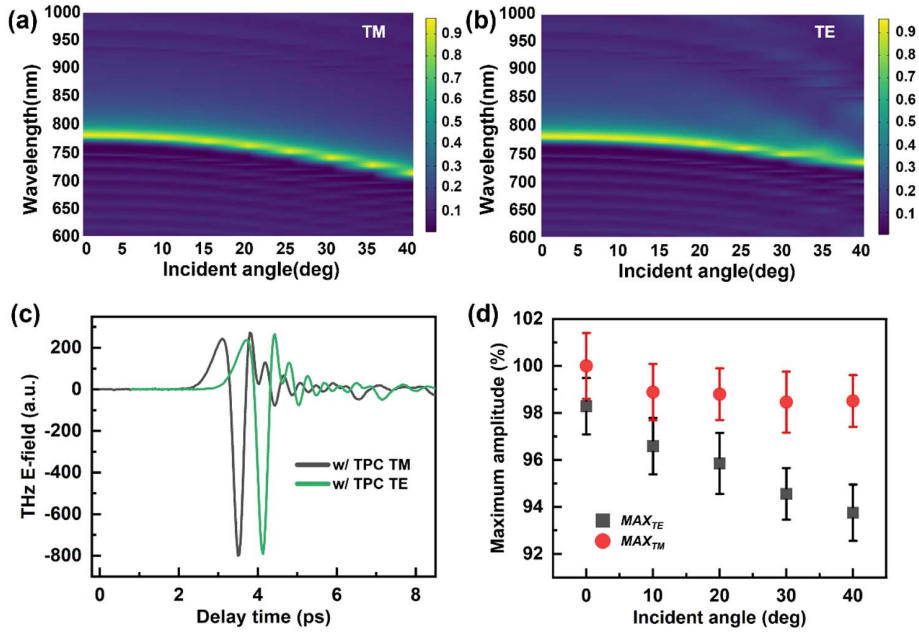

Fig. 5. Absorptance spectra of the spin thin film with TPC under different incident angles and wavelengths for (a) a TM pump beam and (b) a TE pump beam. (c) THz waveforms from the spin thin films with TPC under different polarization states at the pump fluence of 12.7 μJ/cm^2. (d) Normalized maximum amplitude of THz waveforms from the spin thin films with TPC for a TM pump beam and a TE pump beam at different incident angles.

thin films with TPC, while the absorptance is only 0.368 without TPC. To further confirm the absorptance of the samples, the reflectance and transmittance spectra of the different samples are measured by using a spectrometer system, as shown in Fig. 9 in Appendix E. The absorptance spectra were obtained by subtracting the reflectance and transmittance spectra from 1. The measured data are in keeping with the simulation that the TPC brings about a 2.5 times absorptance enhancement compared to the pure spin thin films. Crucially, the pure dielectric layers have total reflectivity at a 780 nm pump laser. In addition, the value of MAX is proportional to the fluence deposited by pump laser, as shown in Fig. 4(e), indicating the linear energy density dependence of the THz electric field in this power section. The tested THz waveforms under different pump power can be found in Fig. 10 in Appendix F. During these tests, the spot diameter of the pump laser is constant at 1 cm.

Another character of TPC is that it can be flexibly excited in both TM and TE polarizations. Figures 5(a) and 5(b) present the simulated absorptance spectra of the spin thin film with TPC under different incident angles and wavelengths for TM and TE pump beams. With the incident angle increase from 20° to 40°, the responding pump wavelength of TPC appears to have a slight blue shift. Note that the absorptance for the 780 nm wavelength from 0° to 40° is still higher than that of the pure spin thin films since the TPC state excites a stronger resonance coupling. The incident angle, especially from 0° to 20°, continues to have a high absorptance tolerance. Significantly, the simulation absorptances in both the TM polarization and TE polarization are almost invariant at the same incident angle. In Fig. 5(c), the THz radiation experiments under both TM and TE polarization states are presented at a 0° incident pump laser beam, where the maximum amplitudes under TM and TE polarization states are MAX_{TM} and MAX_{TE}, respectively. Obviously, MAX_{TM} and MAX_{TE} are with no noticeable differences in Fig. 5(c), which are 1072 and 1056, respectively. Figure 5 shows the normalized maximum amplitude of THz waveforms from the spin thin films with TPC for TM and TE pump beams at different incident angles. In Fig. 5(d), the variation in the normalized MAX value under TE polarization is related to the incident angle of the pump laser from 0° to 40°. For the TM polarization, there is an acceptable reduction by varying the incident angle. All THz waveforms by varying incident angles are exhibited in Fig. 11 in Appendix G. Therefore, it can be seen that the experiments of the oblique incidence for the spin thin films with TPC are almost consistent with the simulation trend.

3. CONCLUSION

By combining spin thin films with a photonic crystal, a TPC state is established between them by theoretical simulation and experimental fabrication, significantly reducing the pump energy consumption. By adjusting the optical parameters, the designed structure possesses a significant photonic resonance absorption peak at the pump laser wavelength of 780 nm. Compared to the 36.8% absorptance of the pure spin thin films, 94.3% of the energy of the pump laser is trapped within the microcavity and absorbed by the spin thin films with TPC. Experimental results show that the THz electric field is enhanced nearly three times for the spin thin films with TPC. The dielectric layers as a photonic band gap offer a 98%

reflectivity for the pump laser and a 95% transmission for the generated THz wave. Moreover, our design can provide a TPC polarization independent state and remain at a high absorptance under a multidirectional incident pump laser. Using a TPC to reduce the THz radiation consumption can also be easily adapted to other STE designs, greatly expanding the new avenues for THz radiation enhancement.

APPENDIX A: TRANSFER MATRIX METHOD FOR THE 1D PHOTONIC CRYSTAL AND THE SPIN THIN FILMS

To demonstrate the TPC between the spin thin films and the 1D photonic crystal, we modeled the optical reflectance and absorptance of the system based on the transfer matrix method. Derived from Maxwell's equations and boundary conditions, the amplitudes of the electrical and magnetic field of the wave in the front and back interfaces of the m-th layer can be expressed as [44,45]

$$\begin{pmatrix} E_m \\ H_m \end{pmatrix} = M_m \begin{pmatrix} E_{m-1} \\ H_{m-1} \end{pmatrix}, \tag{A1}$$

where M is a transfer matrix with

$$M_m = \begin{bmatrix} \cos(k_m d_m) & -i\eta_m \sin(k_m d_m) \\ -i/\eta_m \sin(k_m d_m) & \cos(k_m d_m) \end{bmatrix}. \tag{A2}$$

Here, k_m, η_m and d_m are the wave vector, the impedance, and the thickness of the m-th layer, respectively. Thus, the transfer matrix of the N-layer's 1D photonic crystal can be expressed as

$$M = \prod_{m=1}^{N} M_m = \begin{pmatrix} m_{11} & m_{12} \\ m_{21} & m_{22} \end{pmatrix}. \tag{A3}$$

The field amplitudes of the input and output waves in the one-dimensional photonic crystal can be characterized by the transfer matrix $\begin{pmatrix} E_o \\ H_o \end{pmatrix} = M \begin{pmatrix} E_i \\ H_i \end{pmatrix}$. Then the transmission and reflection coefficients of the system can be calculated as

$$r = \frac{m_{11}\eta_0 - m_{22}\eta_0 + m_{12} - m_{21}\eta_0^2}{m_{11}\eta_0 + m_{22}\eta_0 + m_{12} + m_{21}\eta_0^2}, \tag{A4}$$

$$t = \frac{2\eta_0}{m_{11}\eta_0 + m_{22}\eta_0 + m_{12} + m_{21}\eta_0^2}. \tag{A5}$$

On the other hand, because the spin thin films are composed of a Pt(4 nm)/Co(4 nm)/MgO(4 nm) multilayer heterostructure, the transfer matrix of this system is $M = M_{\mathrm{Mgo}} \cdot M_{\mathrm{Co}} \cdot M_{\mathrm{Pt}}$, where M_{Mgo}, M_{Co}, and M_{Pt} are the transfer matrix of the MgO layer, Co layer, and Pt layer, and they can be calculated by the Eq. (A3), respectively. Then, based on Eqs. (A4) and (A5), the transmission and reflection coefficients of the spin thin films also can be calculated.

APPENDIX B: SIMULATED TRANSMITTANCE OF THz WAVE ON THE DIELECTRIC LAYERS

The simulated transmittance for the THz wave on the dielectric layers obtains 95%, and 96.35% within 2 THz in Fig. 6. It can be seen that the dielectric layers have little influence on the transmission and frequency of THz wave.

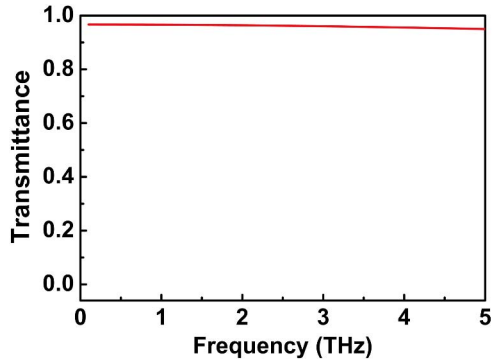

Fig. 6. Simulated transmittance of THz wave on the dielectric layers.

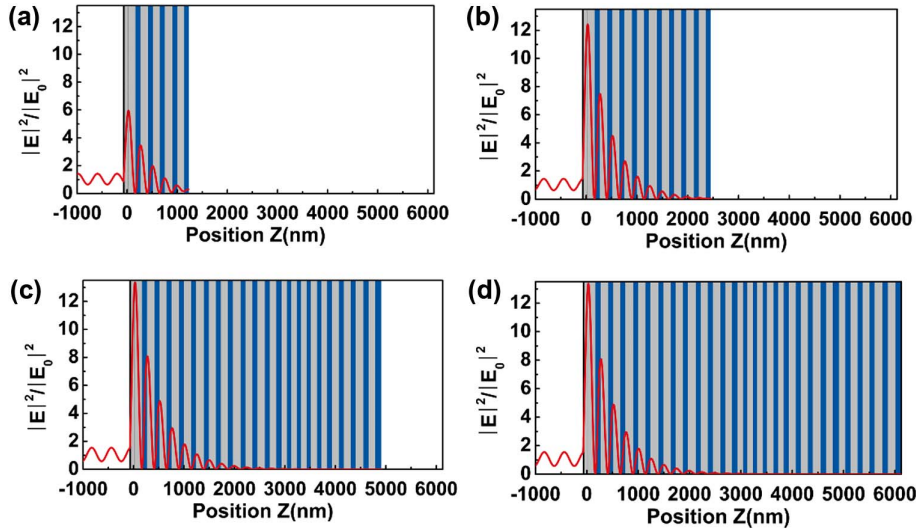

Fig. 7. Normalized electric field profile distributions of (a) five groups, (b) 10 groups, (c) 20 groups, and (d) 25 groups of alternating layers.

APPENDIX C: NORMALIZED ELECTRIC FIELD PROFILE DISTRIBUTIONS

With the increment of alternating layers, the electric field intensity increases before 20 groups, but approaches saturation after that number of groups. Thus, 20 groups of alternating layers are selected as a balanced consideration between the optical performance and simple preparation.

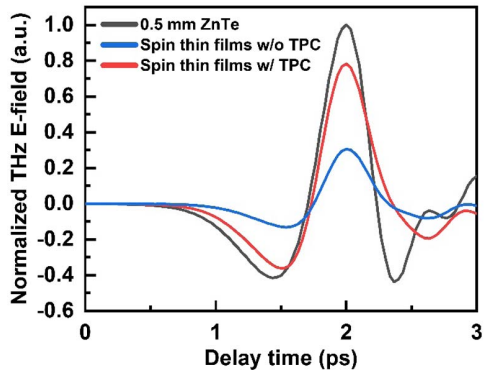

Fig. 8. THz waveforms from 0.5 mm thick ⟨110⟩ cut ZnTe (black line), the spin thin films without TPC (blue line), the spin thin films with TPC (red line) at the pump fluence of 5 μJ/cm^2. All the samples were tested in air.

APPENDIX D: COMPARISON WITH ZnTe CRYSTAL

The normalized THz amplitudes of 0.5 mm ZnTe, spin thin films without TPC and with TPC are compared in Fig. 8. Note that spin thin films with TPC have an approximate value compared to the 0.5 mm thick ZnTe THz emitter.

APPENDIX E: REFLECTANCE, TRANSMITTANCE, AND ABSORPTANCE

To further confirm the absorptance of the samples, the reflectance and transmittance spectra of the different samples are measured by using a spectrometer system, as shown in Fig. 9. The TPC brings about a 2.5 times absorptance enhancement compared to the pure spin thin films.

APPENDIX F: THz WAVEFORMS UNDER DIFFERENT LASER POWERS

All of tested THz time domain waveforms under different pump power can be found in Fig. 10, which shows that the value of MAX is proportional to the fluence deposited by pump laser.

APPENDIX G: THz WAVEFORMS AT DIFFERENT INCIDENT ANGLES

All THz waveforms by varying incident angles are exhibited in Fig. 11, which shows that the experiments of the oblique

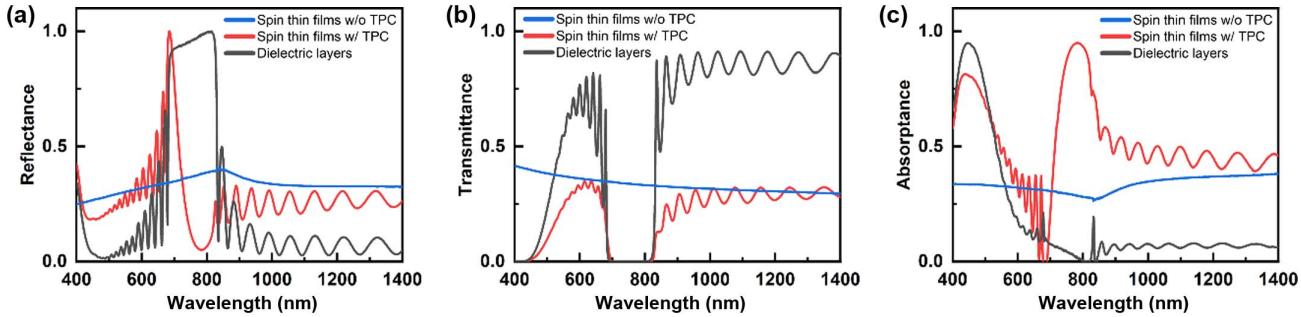

Fig. 9. (a) Reflectance, (b) transmittance, and (c) absorptance spectra of pure spin thin films (spin thin films without TPC, blue line), spin thin films with TPC (red line), and pure dielectric layers (black line).

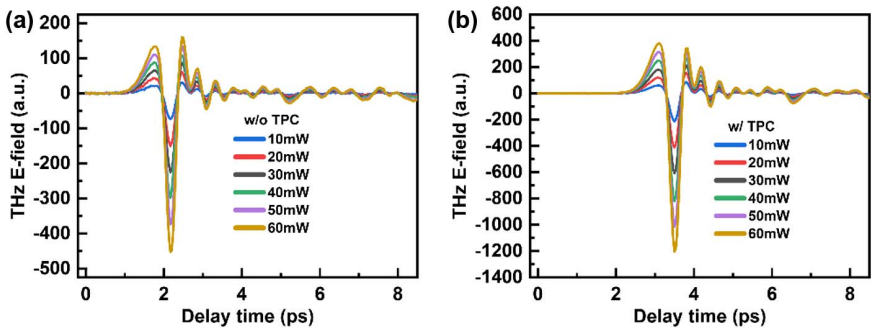

Fig. 10. THz waveforms from the spin thin films: (a) without TPC and (b) with TPC as a function of laser power when the spot diameter is 1 cm.

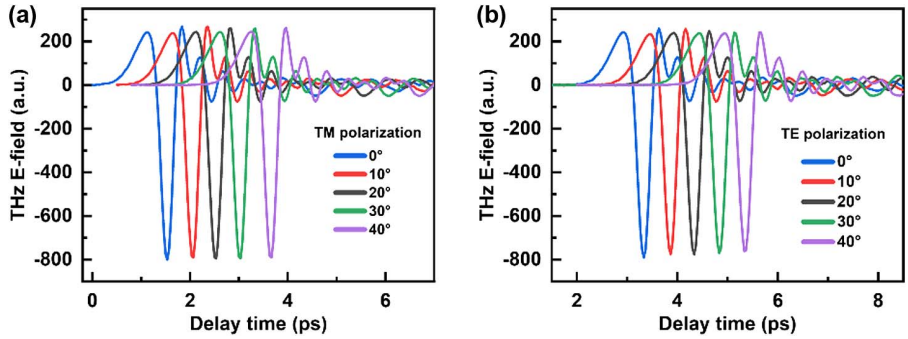

Fig. 11. THz waveforms at 12.7 μJ/cm^2 from spin thin films with TPC under (a) a TM polarization state and (b) a TE polarization state at different incident angles.

incidence for the spin thin films with TPC are almost consistent with the simulation trend.

Funding. Beihang Hefei Innovation Research Institute Project (BHKX-19-01); National Natural Science Foundation of China (12004025).

Acknowledgment. Y. Xiao acknowledges support from the cultivation projects of National Major R&D Project (92164108) and the Foundation of Innovation Center of Radiation Application (KFZC2020020901).

Disclosures. The authors declare that there are no conflicts of interest related to this paper.

Data Availability. Data underlying the results presented in this paper are not publicly available at this time but may be obtained from the authors upon reasonable request.

REFERENCES

1. S. Pirandola, B. R. Bardhan, T. Gehring, C. Weedbrook, and S. Lloyd, "Advances in photonic quantum sensing," Nat. Photonics **12**, 724–733 (2018).
2. L. Chen, Q. Ma, Q. F. Nie, Q. R. Hong, H. Y. Cui, Y. Ruan, and T. J. Cui, "Dual-polarization programmable metasurface modulator for near-field information encoding and transmission," Photon. Res. **9**, 116–124 (2021).
3. B. Dieny, I. L. Prejbeanu, K. Garello, P. Gambardella, P. Freitas, R. Lehndorff, W. Raberg, U. Ebels, S. O. Demokritov, J. Akerman, A. Deac, P. Pirro, C. Adelmann, A. Anane, A. V. Chumak, A. Hirohata, S. Mangin, S. O. Valenzuela, M. C. Onbaşli, M. d'Aquino, G. Prenat, G. Finocchio, L. Lopez-Diaz, R. Chantrell, O. Chubykalo-Fesenko, and P. Bortolotti, "Opportunities and challenges for spintronics in the microelectronics industry," Nat. Electron. **3**, 446–459 (2020).
4. N. T. Bagraev, P. A. Golovin, V. S. Khromov, L. E. Klyachkin, A. M. Malyarenko, V. A. Mashkov, B. A. Novikov, A. P. Presnukhina, A. S. Reukov, and K. B. Taranets, "Terahertz emitters based on negative-U materials for medical applications," Mater. Phys. Mech. **44**, 264–270 (2020).
5. J. Li, G. Wang, Z. Yue, J. Liu, J. Li, C. Zheng, Y. T. Zhang, Y. Zhang, and J. Yao, "Dynamic phase assembled terahertz metalens for reversible conversion between linear polarization and arbitrary circular polarization," Opto-Electron. Adv. **5**, 210062 (2022).
6. O. Gueckstock, L. Nádvorník, T. S. Seifert, M. Borchert, G. Jakob, G. Schmidt, G. Woltersdorf, M. Kläui, M. Wolf, and T. Kampfrath, "Modulating the polarization of broadband terahertz pulses from a spintronic emitter at rates up to 10 kHz," Optica **8**, 1013–1019 (2021).
7. X. Li, T. Qiu, J. Zhang, E. Baldini, J. Lu, A. M. Rappe, and K. A. Nelson, "Terahertz field-induced ferroelectricity in quantum paraelectric $SrTiO_3$," Science **364**, 1079–1082 (2019).
8. Q. Ma and T. J. Cui, "Information metamaterials: bridging the physical world and digital world," Photonix **1**, 1 (2020).
9. G. A. Valdivia-Berroeta, Z. B. Zaccardi, S. K. F. Pettit, E. S. Ho, B. W. Palmer, M. J. Lutz, C. Rader, B. P. Hunter, N. K. Green, C. Barlow, C. Z. Wayment, D. J. Ludlow, P. Petersen, S. J. Smith, D. J. Michaelis, and J. A. Johnson, "Data mining for terahertz generation crystals," Adv. Mater. **34**, 2107900 (2022).
10. Y. Jiang, X. Zhang, Y. Liu, P. Vallobra, S. Eimer, F. Zhang, Y. Du, F. Liu, Y. Xu, and W. Zhao, "Spintronic terahertz emitter with integrated electromagnetic control," Chin. Opt. Lett. **20**, 043201 (2022).
11. X. Zhang, Y. Jiang, Y. Xu, F. Liu, G. Rui, A. Wang, and W. Zhao, "Unidirectional spintronic terahertz emitters with high efficiency," Opt. Lett. **47**, 6381–6384 (2022).
12. C. W. Luo, H.-J. Chen, C. M. Tu, C. C. Lee, S. A. Ku, W. Y. Tzeng, T. T. Yeh, M. C. Chiang, H. J. Wang, W. C. Chu, J.-Y. Lin, K. H. Wu, J. Y. Juang, T. Kobayashi, C.-M. Cheng, C.-H. Chen, K.-D. Tsuei, H. Berger, R. Sankar, F. C. Chou, and H. D. Yang, "THz generation and detection on Dirac fermions in topological insulators," Adv. Opt. Mater. **1**, 804–808 (2013).
13. Y. Li, K. W. Edmonds, X. Liu, H. Zheng, and K. Wang, "Manipulation of magnetization by spin-orbit torque," Adv. Quantum Technol. **2**, 1800052 (2019).
14. X. Wang, L. Cheng, D. Zhu, Y. Wu, M. Chen, Y. Wang, D. Zhao, C. B. Boothroyd, Y. M. Lam, J.-X. Zhu, M. Battiato, J. C. W. Song, H. Yang, and E. E. M. Chia, "Ultrafast spin-to-charge conversion at the surface of topological insulator thin films," Adv. Mater. **30**, 1802356 (2018).
15. M. Tong, Y. Hu, Z. Wang, T. Zhou, X. Xie, X. Cheng, and T. Jiang, "Enhanced terahertz radiation by efficient spin-to-charge conversion in Rashba-mediated Dirac surface states," Nano Lett. **21**, 60–67 (2021).
16. A. Jooshesh, V. Bahrami-Yekta, J. Zhang, T. Tiedje, T. E. Darcie, and R. Gordon, "Plasmon-enhanced below bandgap photoconductive terahertz generation and detection," Nano Lett. **15**, 8306–8310 (2015).
17. F. Cheng, C. Wang, Z. Su, X. Wang, Z. Cai, N. X. Sun, and Y. Liu, "All-optical manipulation of magnetization in ferromagnetic thin films enhanced by plasmonic resonances," Nano Lett. **20**, 6437–6443 (2020).
18. Z. Z. Liu and K. Aydin, "Localized surface plasmons in nanostructured monolayer black phosphorus," Nano Lett. **16**, 3457–3462 (2016).
19. S. Liu, F. Guo, P. Li, G. Wei, C. Wang, X. Chen, B. Wang, W. Zhao, J. Miao, L. Wang, Y. Xu, and X. Wu, "Nanoplasmonic-enhanced spintronic terahertz emission," Adv. Mater. Interfaces **9**, 2101296 (2021).
20. W. Jia, M. Liu, Y. Lu, X. Feng, Q. Wang, X. Zhang, Y. Ni, F. Hu, M. Gong, X. Xu, Y. Huang, W. Zhang, Y. Yang, and J. Han, "Broadband

terahertz wave generation from an epsilon-near-zero material," Light Sci. Appl. **10**, 11 (2021).
21. B. H. Miller, H. Liu, and M. Kolle, "Scalable optical manufacture of dynamic structural colour in stretchable materials," Nat. Mater. **21**, 1014–1018 (2022).
22. Q. Cao, P. Zheng, and Q. Zhan, "Vectorial sculpturing of spatiotemporal wavepackets," APL Photon. **7**, 096102 (2022).
23. L. Hu, B. Wang, Y. Guo, S. Du, J. Chen, J. Li, C. Gu, and L. Wang, "Quasi-BIC enhanced broadband terahertz generation in all-dielectric metasurface," Adv. Opt. Mater. **10**, 2200193 (2022).
24. Y. Lu, X. Feng, Q. Wang, X. Zhang, M. Fang, W. E. I. Sha, Z. Huang, Q. Xu, L. Niu, X. Chen, C. Ouyang, Y. Yang, X. Zhang, E. Plum, S. Zhang, J. Han, and W. Zhang, "Integrated terahertz generator-manipulators using epsilon-near-zero-hybrid nonlinear metasurfaces," Nano Lett. **21**, 7699–7707 (2021).
25. J. H. Kang, H. Wenzel, E. Freier, V. Hoffmann, J. Fricke, O. Brox, M. Matalla, and S. Einfeldt, "Continuous-wave operation of 405 nm distributed Bragg reflector laser diodes based on GaN using 10th-order surface gratings," Photon. Res. **10**, 1157–1161 (2022).
26. T. Liu, C. Yang, Z. Fan, X. Chen, Z. Chen, Y. Su, H. Zhu, F. Sun, T. Jiang, W. Zhu, W. Shen, J. He, H. Zhu, X. Liu, and Y. Yang, "Spectral narrowing and enhancement of directional emission of perovskite light emitting diode by microcavity," Laser Photon. Rev. **16**, 2200091 (2022).
27. M. H. Lee, S. Nellen, F. Soares, M. Moehrle, W. Rehbein, M. Baier, B. Globisch, and M. Schell, "Photonic integrated circuit with sampled grating lasers fabricated on a generic foundry platform for broadband terahertz generation," Opt. Express **30**, 20149–20158 (2022).
28. D. Zhang, Y. Xiang, J. Chen, J. Cheng, L. Zhu, R. Wang, G. Zou, P. Wang, H. Ming, M. Rosenfeld, R. Badugu, and J. R. Lakowicz, "Extending the propagation distance of a silver nanowire plasmonic waveguide with a dielectric multilayer substrate," Nano Lett. **18**, 1152–1158 (2018).
29. J. Wang, Y. Zhu, W. Wang, Y. Li, R. Gao, P. Yu, H. Xu, and Z. Wang, "Broadband Tamm plasmon-enhanced planar hot-electron photodetector," Nanoscale **12**, 23945–23952 (2020).
30. F. Lu, L. Gong, Y. Kuai, X. Tang, Y. Xiang, P. Wang, and D. Zhang, "Controllable optofluidic assembly of biological cells using an all-dielectric one-dimensional photonic crystal," Photon. Res. **10**, 14–20 (2021).
31. Y. Kuai, J. Chen, Z. Fan, G. Zou, J. R. Lakowicz, and D. Zhang, "Planar photonic chips with tailored angular transmission for high-contrast-imaging devices," Nat. Commun. **12**, 6835 (2021).
32. D. O. Ignatyeva, C. S. Davies, D. A. Sylgacheva, A. Tsukamoto, H. Yoshikawa, P. O. Kapralov, A. Kirilyuk, V. I. Belotelov, and A. V. Kimel, "Plasmonic layer-selective all-optical switching of magnetization with nanometer resolution," Nat. Commun. **10**, 4786 (2019).
33. Y. Chen, D. Zhang, L. Zhu, R. Wang, P. Wang, H. Ming, R. Badugu, and J. R. Lakowicz, "Tamm plasmon- and surface plasmon-coupled emission from hybrid plasmonic-photonic structures," Optica **1**, 407–413 (2014).
34. J. Yang, H. Zhang, T. Wang, I. De Leon, R. P. Zaccaria, H. Qian, H. Chen, and G. Wang, "Strong coupling of Tamm plasmons and Fabry-Perot modes in a one-dimensional photonic crystal heterostructure," Phys. Rev. Appl. **18**, 014056 (2022).
35. T. Kampfrath, M. Battiato, P. Maldonado, G. Eilers, J. Notzold, S. Mahrlein, V. Zbarsky, F. Freimuth, Y. Mokrousov, S. Blugel, M. Wolf, I. Radu, P. M. Oppeneer, and M. Munzenberg, "Terahertz spin current pulses controlled by magnetic heterostructures," Nat. Nanotechnol. **8**, 256–260 (2013).
36. T. Seifert, S. Jaiswal, U. Martens, J. Hannegan, L. Braun, P. Maldonado, F. Freimuth, A. Kronenberg, J. Henrizi, I. Radu, E. Beaurepaire, Y. Mokrousov, P. M. Oppeneer, M. Jourdan, G. Jakob, D. Turchinovich, L. M. Hayden, M. Wolf, M. Münzenberg, M. Kläui, and T. Kampfrath, "Efficient metallic spintronic emitters of ultrabroadband terahertz radiation," Nat. Photonics **10**, 483–488 (2016).
37. W. S. M. Werner, K. Glantschnig, and C. Ambrosch-Draxl, "Optical constants and inelastic electron-scattering data for 17 elemental metals," J. Phys. Chem. Ref. Data **38**, 1013–1092 (2009).
38. R. E. Stephens and I. H. Malitson, "Index of refraction of magnesium oxide," J. Res. Natl. Bur. Stand. **49**, 249–252 (1952).
39. D. Kim, Y. W. Oh, J. U. Kim, S. Lee, A. Baucour, J. Shin, K. J. Kim, B. G. Park, and M. K. Seo, "Extreme anti-reflection enhanced magneto-optic Kerr effect microscopy," Nat. Commun. **11**, 5937 (2020).
40. X. Wang, X. Jiang, Q. You, J. Guo, X. Dai, and Y. Xiang, "Tunable and multichannel terahertz perfect absorber due to Tamm surface plasmons with graphene," Photon. Res. **5**, 536–542 (2017).
41. Y. M. Qing, H. F. Ma, and T. J. Cui, "Flexible control of light trapping and localization in a hybrid Tamm plasmonic system," Opt. Lett. **44**, 3302–3305 (2019).
42. Y. Wu, M. Elyasi, X. Qiu, M. Chen, Y. Liu, L. Ke, and H. Yang, "High-performance THz emitters based on ferromagnetic/nonmagnetic heterostructures," Adv. Mater. **29**, 1603031 (2017).
43. Z. Y. Wang, J. K. Clark, Y. L. Ho, B. Vilquin, H. Daiguji, and J. J. Delaunay, "Narrowband thermal emission realized through the coupling of cavity and Tamm plasmon resonances," ACS Photon. **5**, 2446–2452 (2018).
44. Z. Feng, R. Yu, Y. Zhou, H. Lu, W. Tan, H. Deng, Q. Liu, Z. Zhai, L. Zhu, J. Cai, B. Miao, and H. Ding, "Highly efficient spintronic terahertz emitter enabled by metal-dielectric photonic crystal," Adv. Opt. Mater. **6**, 1800965 (2018).
45. H. Lu, X. Gan, B. Jia, D. Mao, and J. Zhao, "Tunable high-efficiency light absorption of monolayer graphene via Tamm plasmon polaritons," Opt. Lett. **41**, 4743–4746 (2016).